Mechanical characterization of porcine liver properties for computational simulation of indentation on cancerous tissue

Yingqiao Yang · Kewei Li · Gerhard Sommer · Kai-Leung Yung · Gerhard A. Holzapfel

Abstract An accurate characterization of soft tissue properties is essential for realistic simulation of surgical procedures. Unconfined uniaxial compression tests with specimens affixed to the fixture are often performed to characterize the stress-stretch curves of soft tissues, with which the material parameters can be obtained. However, the constrained boundary condition causes non-uniform deformation during the uniaxial test, posing challenges for accurate measurement of tissue deformation. In this study, we measured the deformation locally at the middle of the specimen and obtained the corresponding stress-stretch curves. Since the effect of the constrained boundary condition on the local deformation of specimen is minimized, the stress-stretch curves are thus more realistic. Subsequently, we fitted the experimental stress-stretch curves with several constitutive models and found that the first-order Ogden hyperelastic material model was most suitable for characterizing the mechanical properties of the porcine liver tissue. To further verify the characterized material properties, we carried out indentation tests on porcine liver specimens and compared the experimental data with the computational results by using finite element simulations. A good agreement was achieved. Finally, we constructed computational models of liver tissue with a tumor and investigated the effect of the tumor on the mechanical responses of the tissue under indentation. The computational results revealed that the liver specimen with tumor shows a stiffer response if the distance between the tumor and the indenter is small.

Keywords Mechanical characterization · Porcine liver · Cancer tissue detection · Finite element modeling · Surgical indentation

Yingqiao Yang
Department of Industrial and Systems Engineering, The Hong Kong Polytechnic University, 1 Yuk Road, Hung Hom, Kowloon, Hong Kong

Kewei Li
Institute of Biomechanics, Graz University of Technology, Stremayrgasse 16-II, 8010 Graz, Austria

Gerhard Sommer
Institute of Biomechanics, Graz University of Technology, Stremayrgasse 16-II, 8010 Graz, Austria

Kai-Leung Yung
Department of Industrial and Systems Engineering, The Hong Kong Polytechnic University, 1 Yuk Road, Hung Hom, Kowloon, Hong Kong

Gerhard A. Holzapfel
Institute of Biomechanics, Graz University of Technology, Stremayrgasse 16-II, 8010 Graz, Austria
Department of Structural Engineering, Norwegian University of Science and Technology, 7491 Trondheim, Norway

1 Introduction

Surgical simulation has been widely employed to assist surgical planning and train new doctors with lower costs and risks. For a realistic simulation of soft tissue deformation and tool–tissue interactions in surgical intervention, accurate mechanical properties of soft tissues are required.

In clinical diagnosis, palpation is a method to examine many diseases, such as the subsurface abnormalities. The procedure is subjective as the outcome often depends on the sensation and experience of individual physician. With the advance of the robotic minimally invasive surgery, many studies have been developing tumor diagnosis methods by using robotic indentation/palpation either based on silicone phantoms or animal organs (Yamamoto et al., [29]; Ahn et al., [1]; Konstantinova et al., [17]). The basic concept is that the cancerous tissue is often stiffer than the healthy tissue, an increase in the reaction force when under indentation may indicate the existence of the tumor or other diseases. However, the property of silicone phantom is often different from the real tissue, and the property of animal organs may change

in different experimental conditions. This limits the applicability and repeatability of the robotic tumor diagnosis.

Development of a computational model for studying cancerous tissue under indentation may provide a better understanding of the impact of the tumor on the overall mechanical behavior of the tissue, and further improve the robotic tumor diagnosis method.

The objective of this study is to acquire accurate material properties of the liver tissue, and apply that data to the cancerous tissue simulation so that we can quantitatively investigate the effects of the tumor on the force-displacement curve of the tissue under indentation. Mechanical characterization of liver tissue properties can be highly beneficial to the treatment of liver diseases (Hawkes et al., [12]). It is generally believed that porcine liver tissues have similar properties to human tissues (Chui et al., [6]). Hence, it is reasonable to investigate the mechanical properties of porcine livers as a first step towards studies on human tissues.

The unconfined uniaxial compression test is an established method for characterizing the nonlinear responses of soft tissues such as the liver (Chui et al., [6]; Hu and Desai, [14]; Gao et al., [11]; Chen et al., [5]), the kidney (Miller, [21]), and the brain (Budday et al., [3]) because the state of the stress induced by the uniaxial compression test is simpler than the indentation and aspiration experiments. If the specimen is not attached to the fixtures firmly at two ends during the uniaxial compression test, the obtained stress-stretch curves may not be accurate enough due to the friction between the specimen and the fixtures. The friction is inevitable and must be accounted for in the characterization of this type of tissues (Wu et al., [28]). Even though many studies have examined the issue of friction in uniaxial tests (Miller, [22]; Rashid et al., [25]), the friction force is difficult to measure and quantify.

An alternative method is to attach the specimen to the fixtures of the testing machine with glue so that a 'no-slip' boundary condition can be achieved. With this method, Chui et al. [6] characterized the properties of porcine liver tissue, and similarly, Budday et al. [3] conducted experiments on human brain tissues. However, they obtained the mechanical properties of soft tissues based on the overall deformation of the specimen, without considering the non-uniform deformation of the specimen caused by the 'no-slip' boundary condition. With the help of glue, the deformation of the specimen becomes non-homogeneous so that the stress-stretch curve based on the deformation of the entire specimen only represents an average response of the specimen. Several researchers have studied the issue of non-homogeneous deformation and proposed different methods to correct the data collected from the tests based on the deformation of the entire specimen. Miller [22] proposed a method to correct the measured stretch ratio of the entire specimen to account for the no-slip condition. Furthermore, Roan and Vemaganti [26] derived a set of correction factors based on extensive finite element (FE) analysis and then corrected the mechanical properties obtained from the deformation of the entire specimen.

In this study, we present an experimental approach that allows us to determine more realistic material properties of porcine liver tissues directly from uniaxial experiments without any corrections. Since Fu and Chui [9] reported that the indentation test involves both compressive and tensile deformation of the tissue and material parameters derived from either uniaxial tension or compression test alone are not accurate enough for computational simulation of liver tissues under indentation tests, we performed both uniaxial tension and compression tests on the same specimen to quantify the mechanical behavior of the liver tissue. During both tests, we use a high-resolution camera to measure the deformation of the specimen only at the middle of the specimen. We then obtained the mechanical properties of the specimen locally. For comparison, we have also measured the deformation of the specimen by using the cross-head displacement of the two fixtures on the testing device. To determine the mechanical parameters of the porcine liver tissue, we fitted the experimental data from both tension and compression tests with five hyperelastic constitutive models. At first, the uniaxial tension and compression testing results were fitted separately, and then the combined data of compression and tension tests were also fitted. Furthermore, we carried out computational simulations of uniaxial and indentation tests to compare with experimental data. The best fitted constitutive model and its verified material parameters were determined and then used in the computational simulation of cancerous liver tissue under indentation test.

2 Materials and Methods

2.1 Specimen preparation and experimental protocol

Intact porcine livers were obtained from a local slaughterhouse in Graz at the time of slaughter and then transported in phosphate-buffered saline (PBS) solution to the laboratory in less than 30 minutes. All tests were performed within 48 h of extraction. Each liver was sliced into thin layers (approx. 10 mm) parallel to the red line shown in Fig. 1. Cylindrical samples with their axial direction along the green arrow in Fig. 1 were cut with a 10 mm biopsy punch and immediately placed in PBS at 4°C. Since the liver tissue is very soft during preparation and mounting, the specimens deformed under their own gravity, leading to a final diameter from 8 to 10 mm and a final length from 7 to 10 mm.

Before the test, we covered the ends of specimen fixtures on the machine with clear and strong adhesive tapes in order to increase the adhesive properties, see Fig. 2(a). Then, we glued the specimen to the fixture with a thin layer of Loctite™ Super Glue, see Fig. 2(b) and (c).

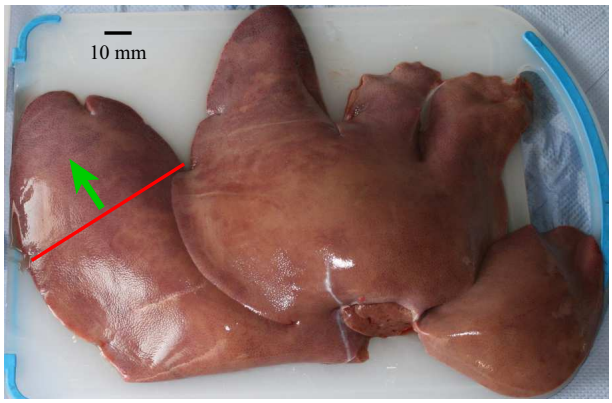

Fig. 1: Fresh porcine liver tissue obtained from a local slaughterhouse. The red line indicates the cutting direction, while the green arrow the axial direction of the cylindrical specimens.

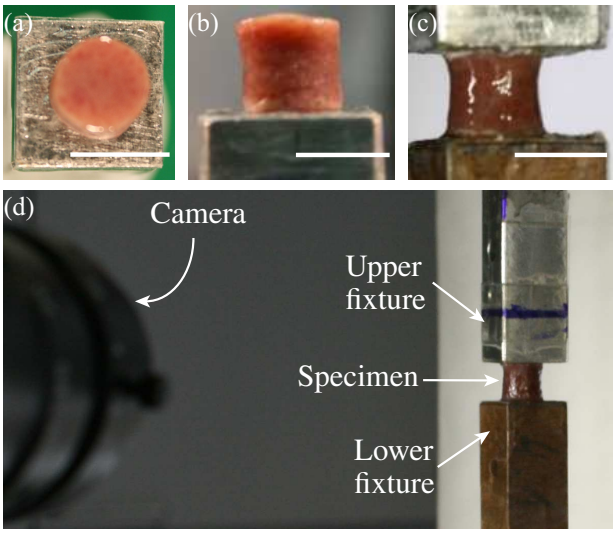

Fig. 2: Cylindrical liver specimen: (a) top view, (b) side view, (c) specimen at the unloaded state between the upper and lower fixtures of the testing machine; (d) experimental setup. The CCD camera was positioned to capture the deformation of interested region on the specimen which was hydrated with PBS during the test. Scale bars indicate 10 mm.

To determine the unloaded state, we first mounted the upper fixture to the testing machine and set the force to zero. Secondly, we glued the specimen to the upper fixture. At this time, the specimen is in a tension state under its own gravity, and the reading from the load cell is the gravity of the specimen with the weight of the glue neglected. Then, we moved the upper fixture together with the specimen downwards to a compressive preload of 0.01 N in order to glue it to the lower fixture. After about 180 s, we gradually reduced the preload to 0 N by moving the upper fixture upwards to obtain the unloaded state, see Fig. 2(c). All tests were conducted at room temperature, and the specimens were hydrated with PBS during the entire test.

Then, we performed the combined compression and tension tests on 13 specimens by firstly compressing the specimen, unloading to its initial load-free configuration and then stretching under tension force. The axial force on the specimen was measured by a 20 N load cell (model Xforce HP 063926, Zwick/Roell group, Ulm, Germany) with an accuracy of 0.2% of the nominal force. The motor control and data acquisition were managed by using the software testXpert II Version 3.2 (Zwick/Roell group, Ulm, Germany). The PC-based videoextensometer (videoXtens, Version 6.4.0.0, Zwick/Roell group, Ulm, Germany) utilizes a CCD camera (model μEye UI-3243-CP-M-GL, IDS, Obersulm, Germany) with a resolution 1280×1024 pixels and a frame rate of 60 fps to measure diameter changes at the middle of the specimen (see Fig. 3). This class 0.5 instrument supports interactive monitor-based selection of the measuring zone and automatically traces gage markers and/or specimen edges using the contrast of the dark liver tissue with respect to the bright background. A maximum error of 0.5% of the field of view, i.e. 0.5% of 20 mm = 0.1 mm, is specified by the manufacturer. The experimental setup is partially shown in Fig. 2(d). Figure 3(a) shows region of interest (between the two green lines), and the measured region (between the two red lines) of the diameter; Fig. 3(b)–(d) show that the diameter changes at tension, unloaded, and compression states, respectively.

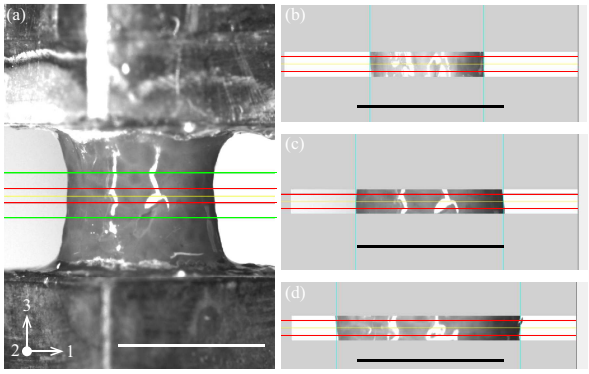

Fig. 3: (a) Unloaded state of the specimen captured by the CCD camera for measurement of the initial diameter in which the interested region is marked by two green lines and the measured region by two red lines; (b) diameter of the specimen under tension; (c) diameter of the specimen at the unloaded state; (d) diameter of the specimen under compression. Scale bars indicate 10 mm.

We performed compression tests up to a nominal strain of 0.3 and tension tests up to a nominal strain of 0.4 according to previous studies (Chui et al., [6]; Gao et al., [11]). We chose a loading speed (cross-head velocity) of 10 mm/min because that was suggested for surgical simulation (Chui et al., [6]). The specimen was tested with five cycles per loading mode, where the first four cycles serve as pre-conditioning and the fifth one for the data analysis. This allowed us to obtain a repeatable and comparable response for all loading modes conducted consecutively on the same specimen. Preliminary investigations had shown that four pre-conditioning cycles were the optimal number to guarantee a repeatable mechani-

cal response while minimizing the risk of tissue damage during the test.

With measured diameter change, the radial stretch λ_1 at the middle of the specimen is determined by using the current diameter divided by the initial diameter. Since the liver tissue is often treated as an incompressible, isotropic, and hyperelastic material, we can thus compute the longitudinal stretch λ_3 (loading direction) at the middle of the specimen within which we assume a homogeneous deformation,

$$\lambda_3 = 1/\lambda_1^2 = 1/\lambda_2^2, \tag{1}$$

where λ_2 is the stretch in the radial direction perpendicular to the camera screen, see Fig. 3(a). With the measured current diameter, the current cross-sectional area at the middle of the specimen can also be determined assuming a circular cross-section during the entire test. The true (Cauchy) stress is then obtained by using the current load divided by the current cross-sectional area. As a result, we obtained the stress-stretch curves locally at the middle of the specimen. In the following, we refer to this as the local method for measuring the mechanical properties. For comparison, we have also computed the stretch λ_3 of the entire specimen by using the displacement of the two fixtures of the testing device at each time step divided by the initial length of the specimen, see Fig. 3(a). The nominal stress component P_{33} in the longitudinal direction was calculated by using the measured force divided by the initial cross-sectional area of the specimen, and then converted to the Cauchy stress σ_{33} in the longitudinal direction by

$$\sigma_{33} = P_{33}\lambda_3. \tag{2}$$

With that, we obtained a second set of Cauchy stress versus stretch curves for the entire specimen. In the following, we refer to this as the global method for measuring the mechanical properties.

After the uniaxial tests, we also performed indentation tests to simulate the procedure in computer-aided surgery. A spherical tipped indenter of 3 mm in diameter was used to indent the tissue at a speed of 10 mm/min to reach a force of 0.12 N, see Fig. 4 for the experiment setup. The reaction force and displacement of the indenter were recorded simultaneously during the indentation test. In total, five specimens with a thickness from 30 to 35 mm were subjected to indentation tests. For each specimen, we performed five indentation tests at five selected points over the central region of the specimen with a relatively flat surface, see Fig. 4. An averaged force-displacement curve was obtained by using all the five tests on all five specimens.

2.2 Constitutive modeling

Abdominal organs such as kidney, liver, and spleen are often considered to be isotropic, hyperelastic, and incompressible

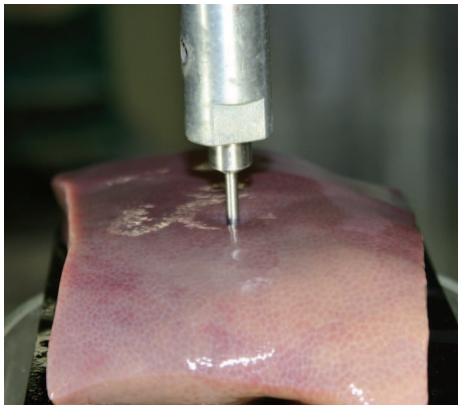

Fig. 4: Indentation test on the porcine liver specimen with a spherical tipped indenter of 3 mm in diameter.

(Humphrey, [15]; Fung [10]). The mechanical response of such materials could be described by using a strain-energy function Ψ defined per unit reference volume. The strain-energy function depends on the state of deformation through the deformation gradient $\mathbf{F}$.

Let now $\mathbf{X}$ be the coordinate of a point in the reference configuration and $\mathbf{x}$ its coordinate in the current configuration. In general, the deformation gradient is given by

$$\mathbf{F} = \frac{\partial \mathbf{x}}{\partial \mathbf{X}}. \tag{3}$$

In the case of uniaxial deformation, the deformation gradient becomes a diagonal tensor [13], which can be written in the matrix form as

$$[\mathbf{F}] = \begin{bmatrix} 1/\sqrt{\lambda} & 0 & 0 \\ 0 & 1/\sqrt{\lambda} & 0 \\ 0 & 0 & \lambda \end{bmatrix}, \tag{4}$$

where $\lambda = \lambda_3$ is the applied stretch in the load direction. The principal invariants of the right Cauchy-Green tensor $\mathbf{C} = \mathbf{F}^{\mathrm{T}}\mathbf{F}$ are

$$I_1 = \lambda^2 + 2/\lambda, \qquad I_2 = 2\lambda + 1/\lambda^2, \qquad I_3 = 1. \tag{5}$$

For strain-energy functions defined in terms of the principal invariants I_1 and I_2, the Cauchy stress $\sigma = \sigma_{33}$ for the uniaxial test is given in [13] as

$$\sigma = 2\frac{\partial \Psi}{\partial I_1}\left(\lambda^2 - \frac{1}{\lambda}\right) + 2\frac{\partial \Psi}{\partial I_2}\left(\lambda - \frac{1}{\lambda^2}\right), \tag{6}$$

while $\sigma_{11} = \sigma_{22} = 0$.

We fitted four widely used hyperelastic strain-energy functions for soft tissues to our experimental data, namely the Mooney-Rivlin (mr) model [23], the Yeoh model [30], the Arruda-Boyce (ab) model [2], and the Ogden (ogd) model [24]. Note that the Mooney-Rivlin model is a special case of the Ogden model. In this study, we used the form of the first-order Ogden model defined in the Abaqus manual [20].

Since the exponential form of the strain-energy function can capture the highly nonlinear behavior of soft tissues, we also considered the Demiray (dmr) model [7]. The strain-energy functions of all five considered hyperelastic models are given as follows:

$$\Psi_{\text{mr}} = C_1(I_1 - 3) + C_2(I_2 - 3), \tag{7}$$

$$\Psi_{\text{yeoh}} = C_1(I_1 - 3) + C_2(I_1 - 3)^2 + C_3(I_1 - 3)^3, \tag{8}$$

$$\Psi_{\text{ab}} = \mu \left[\frac{1}{2}(I_1 - 3) + \frac{1}{20\lambda_m^2}(I_1^2 - 9) + \frac{11}{1050\lambda_m^4}(I_1^3 - 27) + \frac{19}{7000\lambda_m^6}(I_1^4 - 81) + \frac{519}{673750\lambda_m^8}(I_1^5 - 243) \right], \tag{9}$$

$$\Psi_{\text{ogd}} = \frac{2\mu}{\alpha^2}(\lambda_1^\alpha + \lambda_2^\alpha + \lambda_3^\alpha - 3), \tag{10}$$

$$\Psi_{\text{dmr}} = \frac{\mu}{2\beta}\{\exp[\beta(I_1 - 3)] - 1)\}, \tag{11}$$

where μ is the shear modulus, and C_i, α and β are material constants. In (9), λ_m, the locking stretch, is the value of chain stretch when it is fully extended in the polymer. However, in this study, it is treated as a phenomenological parameter.

With equation (6), we can systematically derive the Cauchy stresses for the strain-energy functions defined in terms of principal invariants, i.e.

$$\sigma_{\text{mr}} = 2C_1\left(\lambda^2 - \frac{1}{\lambda}\right) - 2C_2\left(\lambda - \frac{1}{\lambda^2}\right), \tag{12}$$

$$\sigma_{\text{yeoh}} = \left[2C_1 + 4C_2\left(\lambda^2 + \frac{2}{\lambda} - 3\right) + 6C_3\left(\lambda^2 + \frac{2}{\lambda} - 3\right)^2\right]\left(\lambda^2 - \frac{1}{\lambda}\right), \tag{13}$$

$$\sigma_{\text{ab}} = \mu\left[1 + \frac{1}{5\lambda_m^2}\left(\lambda^2 + \frac{2}{\lambda}\right) + \frac{11}{175\lambda_m^4}\left(\lambda^2 + \frac{2}{\lambda}\right)^2 + \frac{19}{875\lambda_m^6}\left(\lambda^2 + \frac{2}{\lambda}\right)^3 + \frac{519}{67375\lambda_m^8}\left(\lambda^2 + \frac{2}{\lambda}\right)^4\right]\left(\lambda^2 - \frac{1}{\lambda}\right), \tag{14}$$

$$\sigma_{\text{dmr}} = \mu \exp\left[\beta(\lambda^2 + \frac{2}{\lambda} - 3)\right]\left(\lambda^2 - \frac{1}{\lambda}\right). \tag{15}$$

In addition, the strain-energy function of the Ogden model depends on the principal stretches. The principal Cauchy stress of the Ogden model under uniaxial test is given in [13], with a slight modification since we are using the Ogden model (10) defined in the Abaqus manual, i.e.

$$\sigma_{\text{ogd}} = \frac{2\mu}{\alpha}\left(\lambda^\alpha - \lambda^{-\alpha/2}\right). \tag{16}$$

For the quantification of the constitutive parameters in each model, we use the nonlinear least-square algorithm in MATLAB and minimize the following objective function

$$\chi^2 = \sum_{i=1}^{n}(\sigma_i - \hat{\sigma}_i)^2, \tag{17}$$

where n is the number of considered experimental data points, σ_i and $\hat{\sigma}_i$ are the experimentally determined and model predicted Cauchy stresses, respectively. In order to compare the performance of the five constitutive models at different loading modes, we first fitted the constitutive models with a single loading mode of compression or tension, and then with the combined loading of compression and tension. For each model, the maximum iteration number was 1000 and the termination tolerance was set to be 10^{-6}. The coefficient of determination r^2 was used to evaluate the goodness of fit. Considering the nonlinear least square algorithm may get stuck in a local minimum, we randomly chose 30 parameter sets as the starting points and determined the final optimal model parameters according to the goodness of fit.

2.3 Computational analysis of the uniaxial and indentation tests

With the obtained material parameters, we developed computational models to simulate the specimen under the uniaxial and indentation tests. FE analyses of the uniaxial compression and tension tests were conducted by using the general purpose FE software Abaqus (Dassault Systèmes SIMULIA Corp., Johnston, RI, USA). As shown in Fig. 5(a), the liver specimen was modeled as a deformable cylinder with 10 mm both in height and diameter, and the upper and lower fixtures were modeled as rigid bodies. The liver model was meshed with 38 400 hexahedral C3D8H elements and 1 920 wedge C3D6H elements. Figure 5 shows the mesh (half) of the liver model. Convergence tests were carried out to determine an appropriate mesh size. The contact between the two fixtures and the specimen was defined as tie constraint to simulate the glued boundary condition.

The loading was applied incrementally as a displacement boundary condition on the upper fixture. Because the resulted stress distribution in the model is non-uniform, the diameter change at the middle of the model (indicated by the red line in Fig. 5) was extracted from the simulation result at each step. Similarly to the experiment, the stretch in the z-axis was then computed from the stretch in the x-axis. The Cauchy stress was then calculated as the reaction force divided by the current cross-sectional area. The Cauchy stress versus stretch curve obtained from the computational simulation was compared with experimental data.

In addition, we also developed computational models of the indentation tests and compared the force-displacement

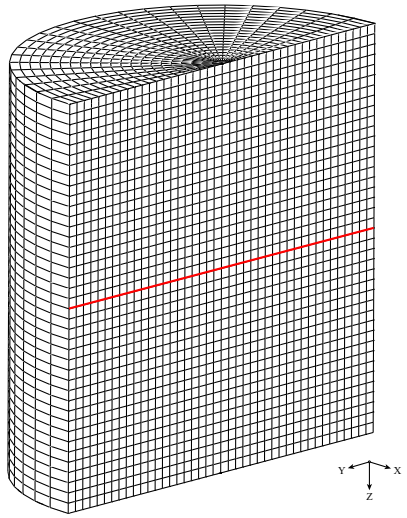

Fig. 5: FE model (only half-model shown) of the liver tissue for simulation of compression and tension tests.

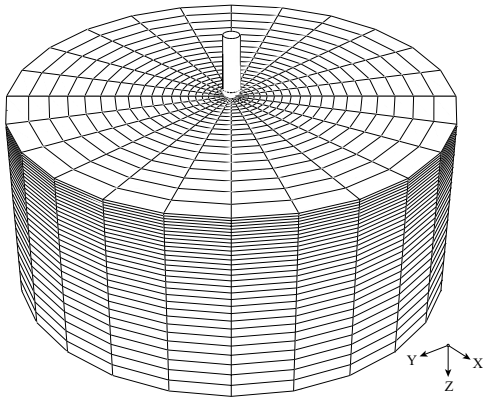

Fig. 6: FE model of the healthy liver tissue with an indenter in the reference configuration for the simulation of the indentation test. The bottom face of the model was fully constrained. A force was applied on the indenter to impose an indentation on the liver model.

curves from computational simulations with experimental data. As shown in Fig. 6, the indenter is modeled as an analytical rigid body with a hemispherical bottom and a diameter of 3 mm. The liver was modeled as a deformable cylinder with 35 mm in height and 80 mm in diameter. We refined the mesh around the contacting region between the indenter and the tissue. The contact between the indenter and the tissue was defined as a frictionless surface-to-surface contact and the bottom face of the liver model was constrained in all three transnational degrees of freedom.

2.4 Computational analysis of cancerous tissue under indentation

In this section, we developed a computational model to investigate the effects of the tumor on the mechanical behavior of a cancerous liver tissue under indentation.

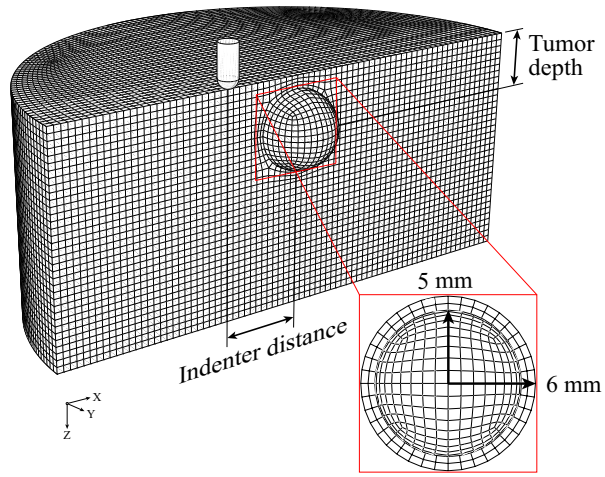

Fig. 7: FE model of the cancerous tissue (only half-model shown) with indenter in the reference configuration. The mature tumor tissue with a layer of the immature tumor is assumed to be in a spherical shape.

The geometry of the FE model is similar to that in Section 2.3 except that we added the cancerous tissue inside the healthy tissue, see Fig. 7. The cancerous tissue is modeled as a spherical body embedded inside the healthy tissue at different depth. The diameter of the spherical body is 10 mm, and it is surrounded by a thin layer of immature cancerous tissue with a thickness of 1 mm, as shown in Fig. 7. Thus, the total diameter of the cancerous tissue is 12 mm. In this study, we assume that the cancerous tissue is linear, elastic, isotropic, and (nearly) incompressible. A Poisson's ratio of 0.499 was adopted in the computational model. The Young's modulus of the mature cancerous tissue was set to 0.74 MPa according to Carter et al. [4]. The Young's modulus of the thin immature cancerous tissue was assumed to be 0.34 MPa empirically, softer than mature cancerous tissue and stiffer than the healthy tissue, to achieve a smoother transition in stress response to the indentation. For more accurate modeling of cancerous tissues, further study should focus on the characterization of cancerous tissue properties and tumor growth, which is beyond the scope of this study. The first-order Ogden model with material parameters obtained from experiment was chosen for the healthy liver tissue in the FE model. As shown in Fig. 7, the radial distance between the center of the tumor tissue and the indenter tip in the reference configuration is defined as the indenter distance, and the vertical distance between the center of the tumor tissue and the top surface of the liver model is defined as the tumor depth. The cancerous tissue was meshed with 408 433 hexahedral C3D8RH elements. In the computational simulation, a gravitational force was firstly exerted on the model, and then a vertical displacement of 10 mm is imposed on the indenter to induce an indentation on the tissue. Convergence tests were carried out to determine an appropriate mesh size.

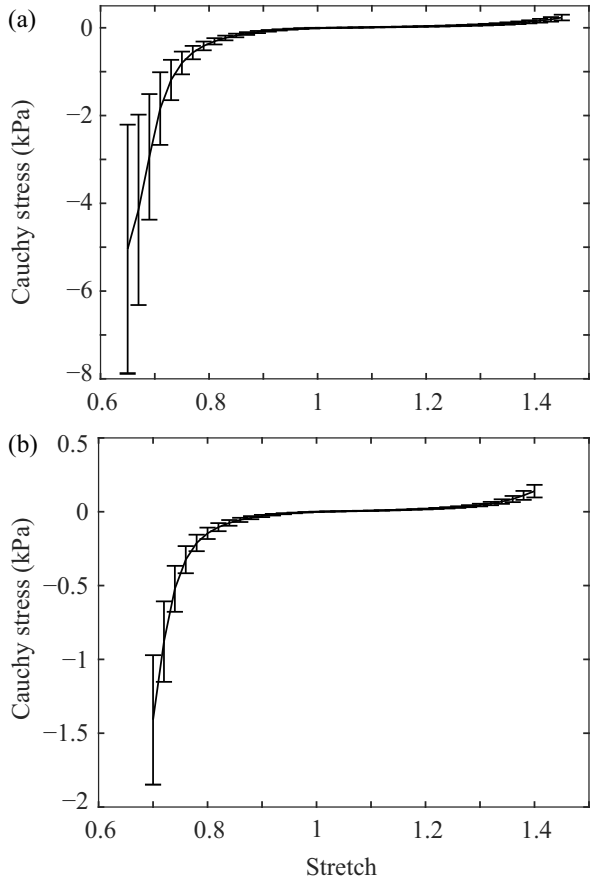

Fig. 8: Averaged experimental stress-stretch curves (mean and standard error). Stress-stretch curves computed by using (a) the local and (b) the global methods for measuring the deformation.

3 Results

3.1 Constitutive parameters

After the experimental tests, we computed an averaged stress-stretch curve from all the 13 porcine liver specimens. The averaged Cauchy stress versus stretch curve (mean and standard error) computed by using the local method for measuring the deformation is shown in Fig. 8(a). For comparison, we also plotted the Cauchy stress versus stretch curve (mean and standard error) by using the global method for measuring the deformation, see Fig. 8(b). As can be seen, when the stretch of the specimen in the loading direction is 0.7 under compression and 1.4 under tension determined by the global method, the stretch at the middle of the specimen is 0.65 under compression and 1.45 under tension, indicating the non-homogeneous deformation of the specimen.

Then, we compared the fitting results of the constitutive models, as introduced in Section 2.2, to the experimental data measured by using the local method (Fig. 9(a)-(c)) and the global method (Fig. 9(d)-(f)). Table 1 summarizes the determined coefficients of each material parameter as well as the goodness of fit for each constitutive model. For the single loading mode with either compression or tension, we obtained good fits with the Yeoh, Ogden and Demiray models. But for the combined compression and tension loading curves, only the Ogden model was able to fit the curves properly, see Fig. 9(c) and Fig. 9(f). Within the tested range, we observed a poor fitting with the Mooney-Rivlin and Arruda-Boyce models for the porcine liver tissue. It should be noted that the Mooney-Rivlin model has a polynomial form and a good fit may be achieved by increasing the order of the model, but that may lead to a over-fitting, which is also reported by Chui et al. [6].

3.2 Simulation of uniaxial test

For the computational simulation of porcine liver tissue under uniaxial tension and compression, we employed the Ogden model with the corresponding material parameters. We defined a material parameter set 'MP1' with $\mu = 0.17\,\text{kPa}$ and $\alpha = -12.25$ determined by the local method, and a second set 'MP2' with $\mu = 0.03\,\text{kPa}$ and $\alpha = -16.46$ determined by the global method under combined loading mode. With material parameter set MP1, we obtained the stress distribution on the axial cross-section of the specimen in the deformed configuration with a stretch ratio of 0.7 and 1.4, see Fig. 10(a) and (b), respectively.

We then extracted the stress-stretch curves from the simulation results by using the method described in Section 2.3, and compared them with the experimental data to verify the accuracy of the material parameters. It should be noted that for the local method the Cauchy stress was calculated directly by using the reaction force divided by the current cross-sectional area of the specimen, while for the global method the nominal stress was calculated first by using the reaction force divided by the initial cross-sectional area of the specimen, and then converted to the Cauchy stress (2). The comparison between the experimental data obtained by the local method with the corresponding computational results by using the parameter set MP1 is shown in Fig. 11(a). Figure 11(b) shows the comparison between the experimental data obtained by the global method, and the computational results with the parameter set 'MP2'. The divergence between experimental data and simulation results, as shown in Fig. 11(b), indicates that the material parameters directly characterized from the deformation of the whole specimen (global method) may not be appropriate for characterizing the tissue properties.

3.3 Simulation of indentation test on healthy liver tissue

Because the porcine liver tissue is very soft, the gravitational force has a non-negligible effect on the tissue deformation. For a more realistic computational simulation of indentation

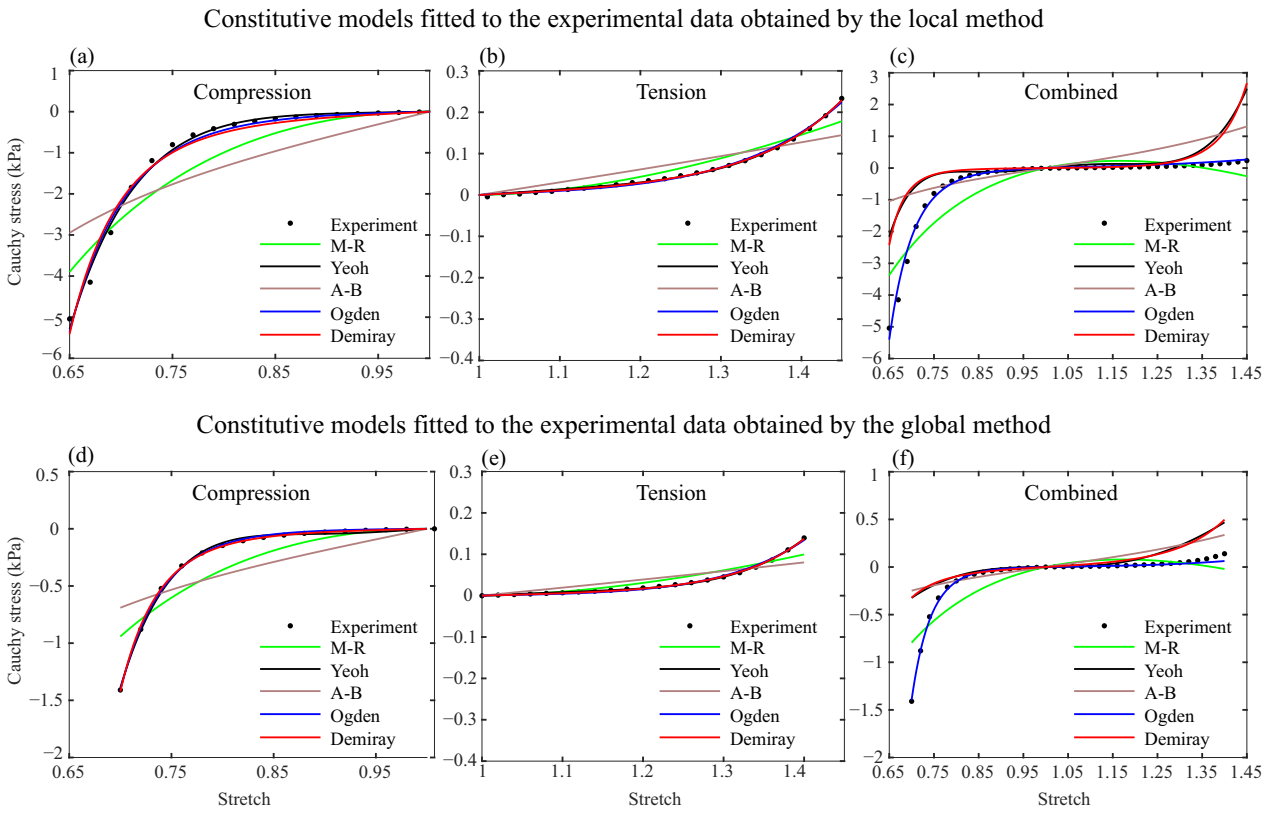

Fig. 9: Comparison of model fit to experimental data: different hyperelastic strain-energy functions (Mooney-Rivlin – M-R, Yeoh, Arruda-Boyce – A-B, Ogden, and Demiray) fitted with averaged experimental data computed by (a)-(c) the local method, and (d)-(f) the global method.

Table 1: Constitutive parameters and r^2 of various models.

Model	Parameter	Compression Test		Tension Test		Combined	
		Local Method	Global Method	Local Method	Global Method	Local Method	Global Method
Mooney–Rivlin	C_1 (kPa)	−3.22	−1.15	0.13	0.20	−1.40	−0.44
	C_2 (kPa)	3.23	1.16	−0.12	−0.19	1.89	0.6
	r^2	0.857	0.795	0.871	0.922	0.794	0.729
Yeoh	C_1 (kPa)	0.24	0.42	0.08	0.06	0.96	0.02
	C_2 (kPa)	0.22	−0.65	−0.001	−0.02	−1	0.29
	C_3 (kPa)	2.79	3.0	0.09	0.13	2.31	−0.09
	r^2	0.993	0.998	0.999	0.999	0.317	0.282
Arruda–Boyce	μ (kPa)	0.73	0.22	0.03	0.02	0.26	0.08
	r^2	0.64	0.567	0.839	0.772	0.196	0.236
Ogden	μ (kPa)	0.19	0.03	0.04	0.02	0.17	0.03
	α (-)	−11.87	−17.28	−22.23	−27.85	−12.25	−16.46
	r^2	0.988	0.999	0.996	0.994	0.989	0.995
Demiray	μ (kPa)	0.42	0.07	0.03	0.02	0.04	0.1
	β (-)	4.9	8.71	3.22	4.86	7.78	3.65
	r^2	0.982	0.999	0.999	0.999	0.327	0.272

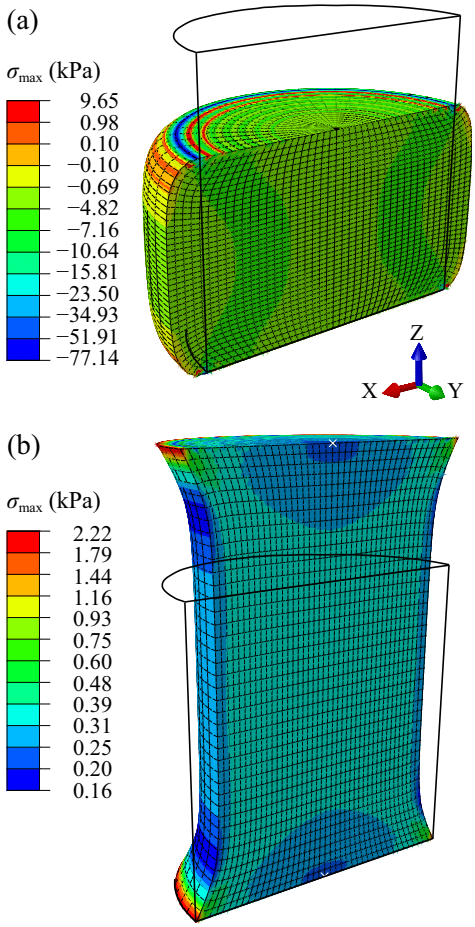

Fig. 10: FE simulation results of uniaxial tests showing the principal (Cauchy) stress (kPa) distribution on the cross-section of the porcine liver model using the Ogden material model and the parameter set MP1: (a) uniaxial compression with stretch ratio 0.7; (b) uniaxial tension with stretch ratio 1.4. Black frames show the reference configurations of the model.

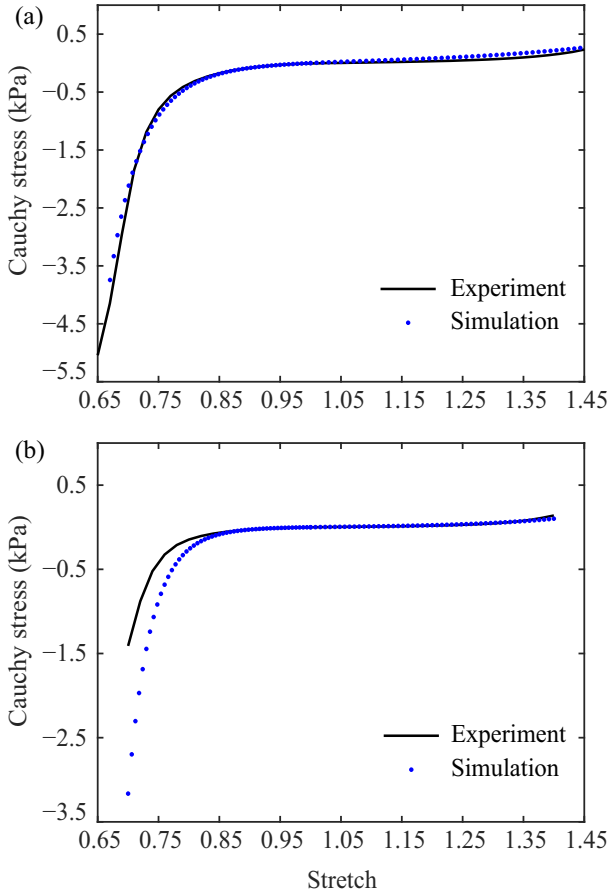

Fig. 11: Comparison of simulation results with experimental data: stress-stretch curve computed by using (a) the local method and (b) the global method.

tests, we first applied a gravitational force on the specimen. The deformation of the specimen under gravity is shown in Fig. 12(a). Subsequently, we applied an indentation force of 0.12 N on the indenter, and the deformed configuration of the specimen is shown in Fig. 12(b). Since the liver tissue deformed under gravity, an initial displacement was required for the indenter to advance to be in contact with the liver model. The actual indentation depth of the indenter, as shown in Fig. 12(b), is the displacement of the tissue under the indenter after they contact with each other. With the material parameter sets MP1 and MP2, we obtained the computational results of the liver tissue specimen under indentation test. Figure 12(c) shows the comparison of applied force versus indentation depth obtained by FE simulations and experimental tests, which further implies that the material parameters characterized by the local method are better for the indentation simulation. Noted that, under the gravitational force, the vertical displacement of the central node on the top face of the liver model is slightly less than the maximum displacement of 3.69 mm shown in Fig. 12(a). Therefore, the actual indentation depth is larger than the difference between the maximum displacement of 8.32 mm shown in Fig. 12(b) and that of Fig. 12(a).

To further investigate the impact of qualifying the material parameters by using combined compression and tension loading modes over that characterized by a single loading mode for indentation simulation, we defined two more parameter sets by using the local method for measuring the deformation at the middle of the specimen under compression mode only: 'MP3' of Yeoh model with $C_1 = 0.24$ kPa, $C_2 = 0.22$ kPa, and $C_3 = 2.79$ kPa, and 'MP4' of Demiray model with $\mu = 4.9$ kPa and $\beta = 0.42$. With those two more parameter sets, we analyzed the deformation of the liver model under indentation tests and extracted the relationship between the force and the indentation depth the computational simulations. The Demiray material model is not a built-in material model in Abaqus; hence we implemented it by using the `Uhyper` user subroutine interface in Abaqus. The results indicate that the force versus indentation

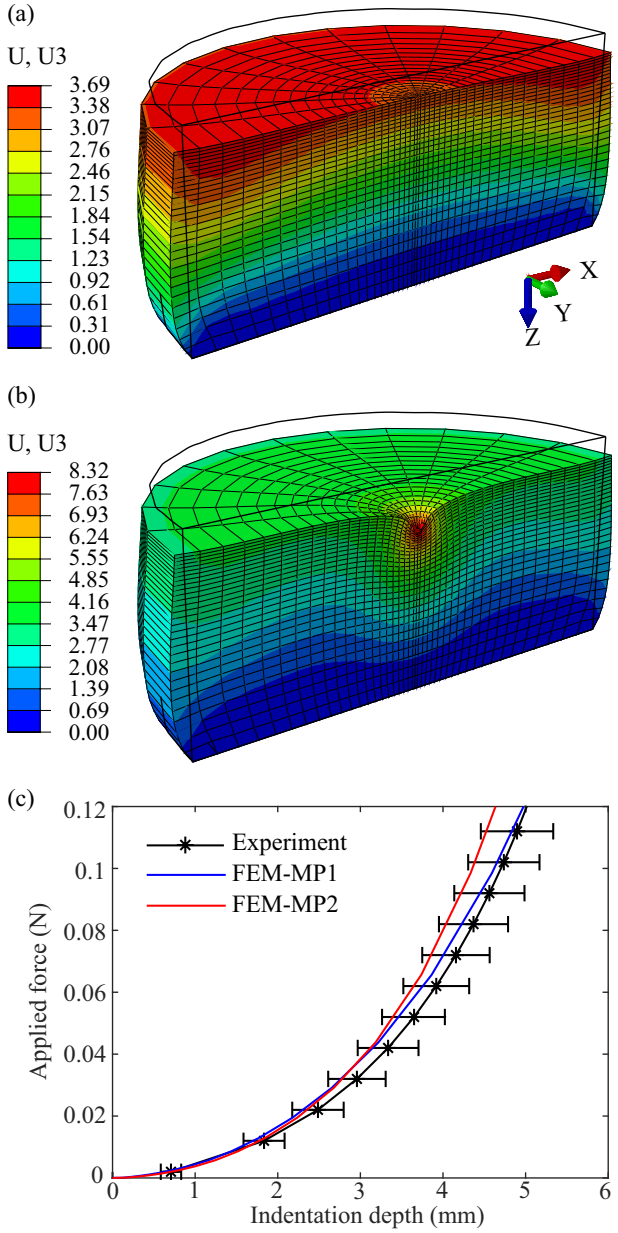

Fig. 12: FE simulation results of liver tissue under indentation tests and comparison with experimental data: (a) deformed cross-section (unit: mm) of the liver tissue under gravitational force only; (b) deformed cross-section under an indentation force of 0.12 N and gravity; (c) comparison of force versus indentation depth between experimental data and simulation results. Black frames show the reference configurations of the model.

depth curves obtained by using the parameter sets MP3 and MP4 also match the experimental data, see Fig. 13. Although we were not able to fit the experimental stress-stretch curve of the combined loading modes with the Yeoh and Demiray models in the tested range, the parameters fitted by using only the compression data are accurate enough for the indentation simulation in the tested range. Therefore, the uniaxial tension test data may not be necessary for simulation of

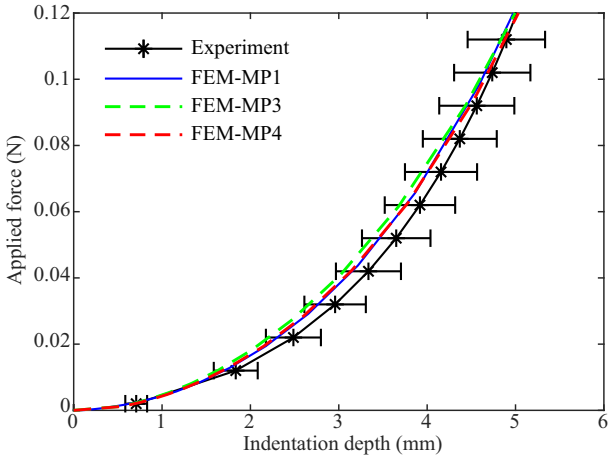

Fig. 13: Comparisons of force versus indentation depth curves between FE simulation results with different material parameter sets and the experimental data of liver tissue under indention test.

indentation tests, while for accurate tissue characterization, combined loading modes are essential.

3.4 Simulation of indentation test on cancerous tissue

The first-order Ogden model with the material parameter set MP1 ($\mu = 0.17$ kPa and $\alpha = -12.25$) was chosen for the healthy part of the cancerous tissue model. Figure 14(a) shows the stress distribution on the FE model with a tumor depth of 13 mm under gravitational force only. The black frame indicates the initial configuration of the model. At first, we investigated the case when the radial distance between the indenter and the tumor is 0 mm, the stress distribution on the model is shown in Fig. 14(b). Then, we investigated the cases when the radial distance between the indenter and the tumor tissue is greater than zero. Figures 14(c) and (d) show the stress distribution on the model with an indenter-to-tumor distance of 6 and 12 mm, respectively. We then extracted the reaction force on the indenter, and the indenter displacement of each case from the FE results, see Fig. 15. As can be seen, with the increase of the radial distance between the indenter and the tumor, the reaction force versus the displacement curve gradually approaches that of the healthy tissue. The correlation between the indenter distance and the reaction force versus the displacement curves can thus be used as an important indicator for surgeons to locate the tumor and other diseases. Note that the reaction force on the indenter is zero in Fig. 15 before contact between the indenter and the liver model is established.

To further investigate the impact of tumor location on the mechanical behavior of the tissue, we developed two more computational models of cancerous tissues with varied tumor depth, i.e. 8 and 18 mm. For each model, we indented the tissue with the indenter distances of 0, 6 and 12 mm. Fig-

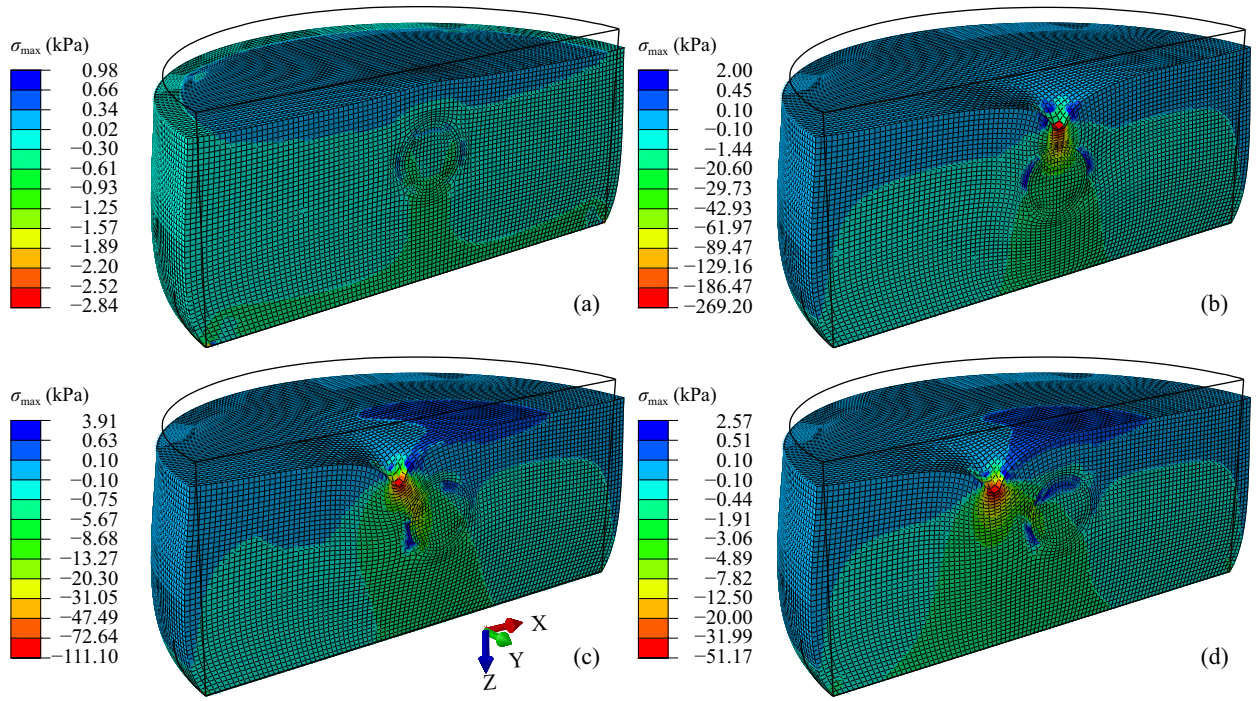

Fig. 14: Maximum principal Cauchy stress (kPa) distribution on the cancerous tissue with a tumor depth of 13 mm: (a) with gravitational force only; (b) with gravity and indentation with an indenter distance of 0 mm; (c) with gravity and indentation, with an indenter distance of 6 mm; (d) with gravity and indentation, with an indenter distance of 12 mm. Black frames indicate the reference configurations of the model. For clarity, the indenter is not shown in the plots.

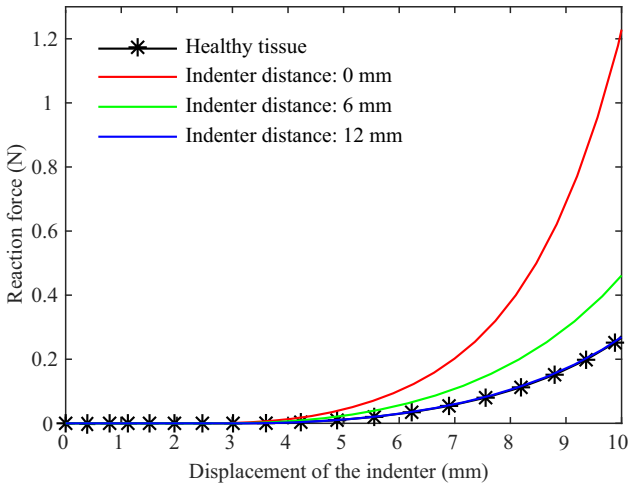

Fig. 15: Force versus displacement curves obtained from the computational simulations of the cancerous liver tissue model under indentation tests with varying indenter-to-tumor distances.

ure 16 shows the force-displacement curve of each case. As shown, when the indenter is right above of the tumor, the force-displacement curve differs the most from that of the healthy tissue, and the magnitude of this difference reduces with the increase of the tumor depth. As the indenter moves away from the tumor, the force-displacement curve gradually approaches that of the normal tissue. With an indenter distance of 6 mm, the force-displacement curves with different tumor depths still diverge from the healthy case but do not vary significantly with respect to the tumor depth. With an indenter distance of 12 mm, the force-displacement curves of all cases are almost identical to the healthy case. In general, with the increase of the tumor depth and the indenter distance, the difference of the force-displacement curve between the healthy and the cancerous tissues reduces, which is reasonable because the deeper and further the tumor is, the more difficult it is to be located.

4 Discussion

In this study, we present a more accurate experimental method for characterizing the mechanical properties of porcine liver tissue by tracking the local deformation of the specimen. This method allows us to measure the deformation locally at the middle of the tissue instead of the overall deformation, which resulted in a more accurate Cauchy stress versus stretch curve. It can also be used to characterize the mechanical properties of other soft tissues such as kidney, spleen, and brain tissues. Before the test, we carefully identified the unloaded state of each specimen so that we can eliminate the effect of gravity, which may explain why the stress-stretch curves we obtained are different from some studies (see, e.g., Roan and Vemaganti, [26]; Chen et al., [5]), where they tested the specimen without a well-defined unloaded state. How-

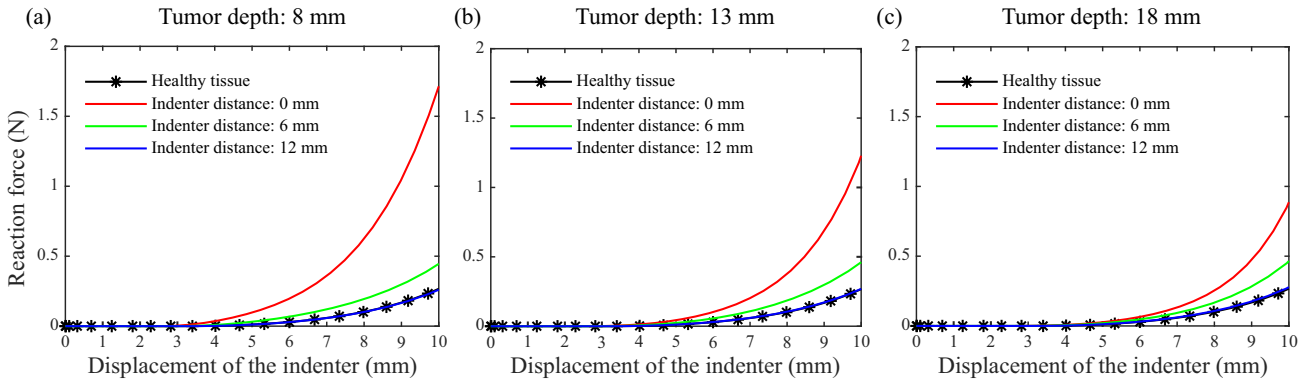

Fig. 16: Force-displacement curves of the healthy and the cancerous tissue under indentation tests with varying indenter distances: (a) tumor depth of 8 mm; (b) tumor depth of 13 mm; (c) tumor depth of 18 mm.

ever, when compared with the work of Chui et al. [6], where the unloaded state was properly considered, we observed a similar magnitude of stress. As for the simulation of cancerous tissue, we investigated the effects of the indenter distance and tumor depth on the force-displacement curve. The strong correlation between the force-displacement curve of the indenter and the location of the tumor can be used as an important indicator for surgeons to locate tumor or other abnormal tissues intra-operatively. Note that the force-displacement curve also depends on the shape and size of the indenter or tumor, as well as the tumor's stiffness. It will be interesting to investigate the optimal combination of indenter size, indenter shape and indentation depth for locating different types of the tumor in a future study.

5 Limitations

One limitation of this study is that the liver tissue was tested at the *in vitro* state. At *in vivo* condition, blood circulation and perfusion are involved so that the mechanical behave may be different. A further study should focus on the measurement of the *in vivo* tissue properties. In addition, shear tests of liver tissues were not performed in this study, which can be benefitial to an accurate characterization of the tissue properties. However, for surgical indentation simulation, uniaxial tests may be enough [6,9,14,26]. If time is considered in the constitutive modeling, the liver tissue may show a viscoelastic behavior [16,19]. Future experiments with different loading rates are required to characterize the viscoelastic properties of tissues. This result can then be integrated into the constitutive model for a more accurate surgical simulation.

In terms of the measurement, we employed a high-resolution CCD camera to measure the strains. The accuracy of measurement can be further improved by employing digital imaging correlation, a full-strain measurement technique, already employed by Gao et al. [11]. But in this paper, the good agreement between computational and experimental results suggests the current measuring technique has achieved an acceptable accuracy.

Furthermore, we did not consider the initial residual stress in the liver tissue. As shown in [8], many biological tissues exhibit considerable initial residual stresses that may affect tissue growth and morphology so that they proposed a model to treat the initial state of biological tissue with residual stress. Future work should focus on quantifying and modeling the initial residual stress of liver tissue for a more accurate simulation.

6 Conclusion

In this study, we present an integrated approach for characterizing the material properties and the computational modeling of porcine liver tissues under various loading conditions. In the uniaxial compression and tension tests, by tracking the deformation of the specimen locally, we obtained more accurate stress-stretch curves of the porcine liver tissue. We also compared the performance of five commonly used constitutive models for characterizing the mechanical behavior of the liver tissue. Our results indicate that the Ogden model is most suitable for capturing the mechanical behavior of porcine liver tissue in the tested range. With the experimentally determined constitutive parameters, we constructed 3D FE models of uniaxial and indentation experiments. The good agreements between simulations and experiments not only validated that the material properties of porcine liver tissue were accurately quantified but also implicated the FE model can realistically capture the deformation of the liver tissue, which will greatly contribute to the realistic soft tissue modeling, especially in the field of surgical simulation. Finally, we simulated the cancerous tissue under indentation and demonstrated the impact of indenter distance and tumor location on the mechanical behavior of the tissue, which may be used to locate the tumor and other

abnormalities in the liver tissue. Future studies with realistic material parameters, patient-specific geometry and location of cancerous tissue could yield more accurate simulation results.

Acknowledgements Y. Y. is financially supported by a research grant from the Hong Kong Polytechnic University (project account code: RUMP) and the Ernst Mach Grant (ICM-2017-08344) from the Centre for International Cooperation and Mobility, Austrian Agency for International Cooperation in Education and Research (OeAD). This support is gratefully acknowledged.

References

1. Ahn, B., Kim, Y., Oh, C.K., Kim, J.: Robotic palpation and mechanical property characterization for abnormal tissue localization. Medical & Biological Engineering & Computing **50**(9), 961–971 (2012)
2. Arruda, E.M., Boyce, M.C.: A three-dimensional constitutive model for the large stretch behavior of rubber elastic materials. Journal of the Mechanics and Physics of Solids **41**(2), 389–412 (1993)
3. Budday, S., Sommer, G., Birkl, C., Langkammer, C., Haybaeck, J., Kohnert, J., Bauer, M., Paulsen, F., Steinmann, P., Kuhl, E., Holzapfel, G.A.: Mechanical characterization of human brain tissue. Acta Biomaterialia **48**, 319–340 (2017)
4. Carter, F.J., Frank, T.G., Davies, P.J., McLean, D., Cuschieri, A.: Measurements and modelling of the compliance of human and porcine organs. Medical Image Analysis **5**(4), 231–236 (2001)
5. Chen, J., Brazile, B., Prabhu, R., Patnaik, S.S., Bertucci, R., Rhee, H., Horstemeyer, M., Hong, Y., Williams, L.N., Liao, J.: Quantitative analysis of tissue damage evolution in porcine liver with interrupted mechanical testing under tension, compression, and shear. Journal of Biomechanical Engineering **140**(7), 071,010 (2018)
6. Chui, C., Kobayashi, E., Chen, X., Hisada, T., Sakuma, I.: Combined compression and elongation experiments and non-linear modelling of liver tissue for surgical simulation. Medical and Biological Engineering and Computing **42**(6), 787–798 (2004)
7. Demiray, H.: A note on the elasticity of soft biological tissues. Journal of Biomechanics **5**(3), 309–311 (1972)
8. Du, Y., Lü, C., Chen, W., Destrade, M.: Modified multiplicative decomposition model for tissue growth: Beyond the initial stress-free state. Journal of the Mechanics and Physics of Solids **118**, 133–151 (2018)
9. Fu, Y., Chui, C.: Modelling and simulation of porcine liver tissue indentation using finite element method and uniaxial stress–strain data. Journal of Biomechanics **47**(10), 2430–2435 (2014)
10. Fung, Y.C.: Biomechanics: mechanical properties of living tissues. Springer Science & Business Media (2013)
11. Gao, Z., Lister, K., Desai, J.P.: Constitutive modeling of liver tissue: experiment and theory. Annals of Biomedical Engineering **38**(2), 505–516 (2010)
12. Hawkes, D.J., Edwards, P.J., Barratt, D., Blackall, J.M., Penney, G.P., Tanner, C.: Measuring and modeling soft tissue deformation for image guided interventions. In: Surgery Simulation and Soft Tissue Modeling, pp. 1–14. Springer (2003)
13. Holzapfel, G.A.: Nonlinear Solid Mechanics: A Continuum Approach for Engineering. John Wiley & Sons Ltd. (2000)
14. Hu, T., Desai, J.P.: Characterization of soft-tissue material properties: large deformation analysis. In: Medical Simulation, pp. 28–37. Springer (2004)
15. Humphrey, J.D.: Continuum biomechanics of soft biological tissues. Proceedings of the Royal Society of London. Series A: Mathematical, Physical and Engineering Sciences **459**(2029), 3–46 (2003)
16. Kerdok, A.E., Ottensmeyer, M.P., Howe, R.D.: Effects of perfusion on the viscoelastic characteristics of liver. Journal of Biomechanics **39**(12), 2221–2231 (2006)
17. Konstantinova, J., Cotugno, G., Dasgupta, P., Althoefer, K., Nanayakkara, T.: Palpation force modulation strategies to identify hard regions in soft tissue organs. PloS one **12**(2), e0171,706 (2017)
18. Lister, K., Gao, Z., Desai, J.P.: Development of in vivo constitutive models for liver: Application to surgical simulation. Annals of biomedical engineering **39**(3), 1060–1073 (2011)
19. Marchesseau, S., Chatelin, S., Delingette, H.: Nonlinear biomechanical model of the liver. In: Biomechanics of Living Organs, pp. 243–265. Elsevier (2017)
20. Dassault Systèmes Simulia Corporation: Abaqus Analysis User's Guide. Johnston, Rhode Island, United States (2014)
21. Miller, K.: Constitutive modelling of abdominal organs. Journal of Biomechanics **33**(3), 367–373 (2000)
22. Miller, K.: Method of testing very soft biological tissues in compression. Journal of Biomechanics **38**(1), 153–158 (2005)
23. Mooney, M.: A theory of large elastic deformation. Journal of applied physics **11**(9), 582–592 (1940)
24. Ogden, R.W.: Large deformation isotropic elasticity–on the correlation of theory and experiment for incompressible rubberlike solids. Proc. R. Soc. Lond. A **326**(1567), 565–584 (1972)
25. Rashid, B., Destrade, M., Gilchrist, M.D.: Determination of friction coefficient in unconfined compression of brain tissue. Journal of the Mechanical Behavior of Biomedical Materials **14**, 163–171 (2012)
26. Roan, E., Vemaganti, K.: The nonlinear material properties of liver tissue determined from no-slip uniaxial compression experiments. Journal of Biomechanical Engineering **129**(3), 450–456 (2007)
27. Snedeker, J.G., Niederer, P., Schmidlin, F., Farshad, M., Demetropoulos, C., Lee, J., Yang, K.: Strain-rate dependent material properties of the porcine and human kidney capsule. Journal of biomechanics **38**(5), 1011–1021 (2005)
28. Wu, J.Z., Dong, R.G., Schopper, A.W.: Analysis of effects of friction on the deformation behavior of soft tissues in unconfined compression tests. Journal of Biomechanics **37**(1), 147–155 (2004)
29. Yamamoto, T., Abolhassani, N., Jung, S., Okamura, A.M., Judkins, T.N.: Augmented reality and haptic interfaces for robot-assisted surgery. The International Journal of Medical Robotics and Computer Assisted Surgery **8**(1), 45–56 (2012)
30. Yeoh, O.H.: Some forms of the strain energy function for rubber. Rubber Chemistry and technology **66**(5), 754–771 (1993)